The Astrophysical Journal Letters, 909:L1 (6pp), 2021 March 1 https://doi.org/10.3847/2041-8213/abe70a

Discovery of Correlated Evolution in Solar Noise Storm Source Parameters: Insights on Magnetic Field Dynamics during a Microflare

Atul Mohan[1,2]
[1] Rosseland Centre for Solar Physics, University of Oslo, Postboks 1029 Blindern, N-0315 Oslo, Norway; atulm@uio.no
[2] Institute of Theoretical Astrophysics, University of Oslo, Postboks 1029 Blindern, N-0315 Oslo, Norway
Received 2020 December 19; revised 2021 February 16; accepted 2021 February 17; published 2021 February 26

Abstract

A solar type-I noise storm is produced by accelerated particle beams generated at active regions undergoing magnetic field restructuring. Their intensity varies by orders of magnitude within subsecond and sub-MHz scales. But the morphological evolution of these sources is not studied at these scales due to the lack of required imaging cadence and fidelity in meterwave bands. Using data from the Murchison Widefield Array, this work explores the coevolution of size, sky-orientation, and intensity of a noise storm source associated with a weak microflare. This work presents the discovery of two correlated modes of evolution in the source parameters: a sausage like "S" mode where the source intensity and size show an anticorrelated evolution; and a torsional like "T" mode where the source size and sky-orientation show a correlated evolution. A flare mediated mode conversion is observed from "T" to "S" for the first time in these sources. These results support the idea of build up of magnetic stress energy in braided active region loops, which later become unstable causing flares and particle acceleration until they relax to a minimally braided state. The discovered mode conversion can be a future diagnostic for such events.

Unified Astronomy Thesaurus concepts: Alfven waves (23); Solar flares (1496); Solar radio flares (1342); Solar active region magnetic fields (1975); Solar active regions (1974); Solar coronal heating (1989); Solar radio emission (1522); Solar x-ray flares (1816); Solar extreme ultraviolet emission (1493); Solar coronal transients (312); Solar oscillations (1515); Solar magnetic reconnection (1504)

1. Introduction

Solar type-I noise storms are usually associated with active regions and sunspots during times of flaring or large-scale magnetic field restructuring (Elgarøy 1977; Kathiravan et al. 2007; Iwai et al. 2011). The bright radio emission is a result of coherent plasma emission mechanisms triggered by flare-accelerated electron beams trapped in active region magnetic field structures (Ginzburg & Zhelezniakov 1958; Melrose & Sy 1972). However, there have been observations of noise storms, especially weak ones with flux enhancements typically less than 100 SFU ($1\mathrm{SFU} = 10^{30}\,\mathrm{W\,m^{-2}\,Hz^{-1}}$), that could not be associated with any particular flares (Smith & McIntosh 1962; Le Squeren 1964). The deciding criteria for a noise storm to occur, and for a flare or active region to be linked to a noise storm are not well understood. Relatively recent works using multiwave band data and sensitive modern radio arrays demonstrated that type-I sources can also be related to small-scale magnetic enhancements and weak Extreme Ultra Violet (EUV) brightening with no necessary flaring or major magnetic field restructuring (e.g., Iwai et al. 2012; Li et al. 2017; Suresh et al. 2017; Mohan et al. 2019a). Since the accelerated electron beams driving the noise storm emission are produced at reconnection sites in these time varying magnetic field structures, their energy and spatial distribution functions are expected to evolve at similar scales (e.g., Gordovskyy & Browning 2012; James & Subramanian 2018; Fyfe et al. 2020). These could leave observable signatures in the noise storm source morphology. However, to study the source dynamics in tandem with its subsecond and sub-MHz scale flux variability (e.g., Wild 1957; Elgaroy & Ugland 1970; Guedel & Benz 1990; Sundaram & Subramanian 2005), high fidelity snapshot spectroscopic imaging at similar scales is essential. This remained a challenge until the advent of modern interferometric arrays like the Murchison Widefield Array (MWA; Tingay et al. 2013), the LOw Frequency ARray (van Haarlem et al. 2013), and the Long Wavelength Array (Ellingson et al. 2013). A similar study was done on type-III bursts by Mohan et al. (2019b). They reported the discovery of second-scale anticorrelated quasi periodic pulsations (QPPs) in the sizes and flux density of type-III sources produced by a weak active region jet. The authors linked it to sausage modes in the active region supported by magnetic field modeling and EUV images of the jet. They also discovered pulsations in the source sky-orientation. This work will present the first study of simultaneous subsecond evolution of noise storm source parameters namely size, sky-orientation, and integrated flux density. The event presented in Mohan et al. (2019a, hereafter M19) is chosen for this study since it is associated with a weak active region transient brightening (ARTB; Shimizu et al. 1992) with no major magnetic field restructuring. Being weak, it can be assumed that several physical parameters remain practically unchanged during the event, increasing the odds for discovering local MHD or plasma perturbative modes. Section 2 describes the observations and image analysis. Section 3 discusses the emergent physical picture from the observed source evolution, followed by conclusions in Section 4.

2. Observations and Analysis

This study is based on archival data, recorded by the MWA Phase I on 2014 November 3 from 06:08:02 to 06:20:02 UT. The observation data sets had a bandwidth of 15.36 MHz, spectral resolution of 40 kHz and time resolution of 0.5 s. Each observing session was 4 minutes long and centered at 199 MHz from 06:08:02–06:12:02, 229 MHz from 06:12:02–06:16:02, and again at 199 MHz 06:16:02–06:20:02. The shift in the

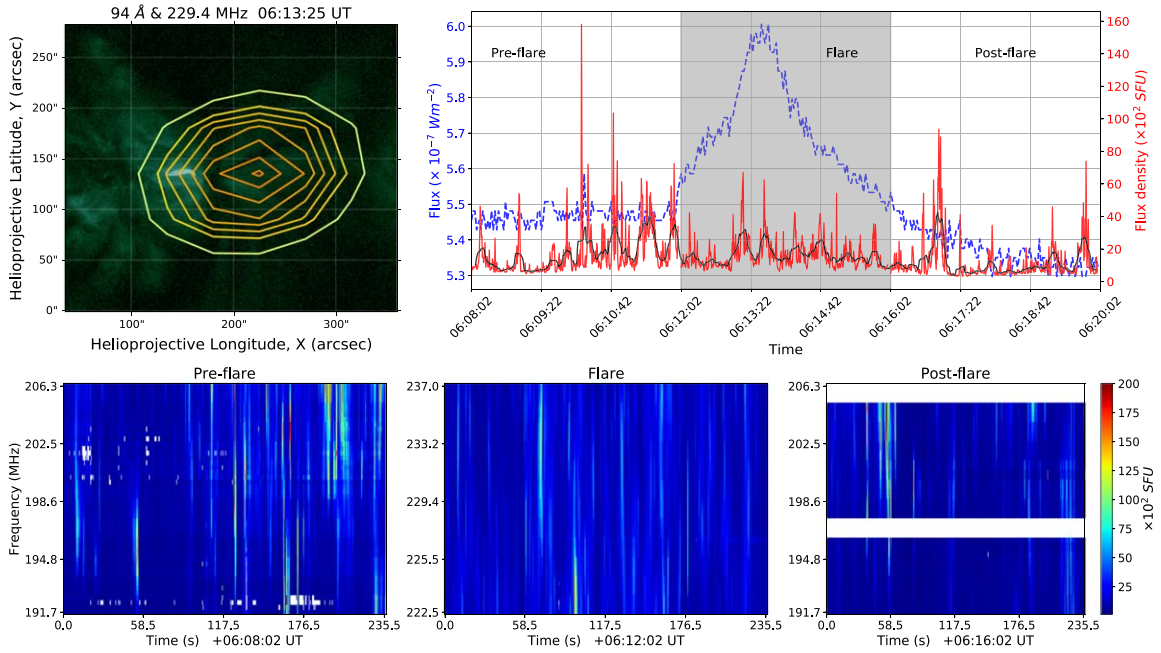

Figure 1. Top row: (left) AIA 94 Å image of the Sun zoomed to the bright ARTB site. Overlaid are MWA 229 MHz contours at 60%, 70%, 75%, 80%, 85%, 90%, 95%, and 99% of the peak noise storm flux. Synthesized beam size: $3\farcm9 \times 2\farcm9$. (Right) Red curve shows the spatially resolved band averaged light curve for the noise storm source. Black curve is a 20 s running mean filtered light curve making 30 s QPPs evident. Overlaid in blue is the GOES 1–8 Å light curve. The three event phases are demarcated. Bottom row: SPatially REsolved Dynamic Spectrum of the source during the three phases.

observation band was not intended for this study. An ARTB event occurred around the middle of the observation period, accompanied by a weak flare detected by RHESSI in the 3–12 keV band. GOES satellites reported a simultaneous B6 class flare. The radio data hence covered the microflare from the pre-flare to the post-flare phase. Imaging was done using the Automated Imaging Routine for Compact Arrays for the Radio Sun (Mondal et al. 2019) at 0.5 s cadence and 160 kHz frequency resolution, using default parameters. The snapshot spectroscopic brightness temperature maps were made using these images following the prescription in Mohan & Oberoi (2017). The noise storm source was resolved in all the images with a size greater than the synthesized beam (beam) by ≈20% on average and had a 2D Gaussian morphology. The left panel of Figure 1 shows noise storm source contours overlaid on an AIA 94 Å image, during the flare. This source has an FWHM of $4\farcm7 \times 3\farcm3$ along its principal axes, when the FWHM of the beam is $3\farcm9 \times 2\farcm9$. The beam-deconvolved source ("true source" hereafter) has ≈37% of the beam size. Using the imfit task of Common Astronomy Software Applications (CASA; McMullin et al. 2007), a 2D Gaussian function plus a constant background was fit to the burst source region in the images across time and frequency. The fitted constant accounted for the quiet Sun background. The beam was deconvolved from the best-fit Gaussian function to derive the true source dimensions: the major and minor axes widths ($\sigma_{\rm major/minor}$); the position angle and the integrated flux density, which is the total flux within the FWHM sized ellipse. Areas of the true sources were estimated as $\pi\sigma_{\rm major}\sigma_{\rm minor}$. The errors on the best-fit parameters were propagated to calculate the errors in area. SPatially REsolved Dynamic Spectra (SPREDS) for the true source was made using the derived integrated flux density. This is shown in the bottom panels of Figure 1. The intermittent white patches show regions where either the data were bad or the estimates were less than thrice the respective fitting errors.

The top right panel of the figure shows a band averaged light curve for the source obtained from SPREDS in red. The black curve is obtained by applying a 20 s wide running mean window. 30 s QPPs can be seen riding over a nonthermal flux floor, which rises during the flare. The GOES X-ray light curve in the 1–8 Å band is shown in blue. The data is divided into three phases based on the flare evolution: Pre-flare, flare, and post-flare. Analysis in the subsequent sections will focus on the spectro-temporal coevolution of the morphological parameters of the noise storm source (area and position angle) in tandem with its integrated flux density during these phases. Earlier studies usually approached the noise storm emission as a bright continuum, superposed with spiky burst features (type-I bursts) (e.g., Mercier & Trottet 1997; Iwai et al. 2014; Suresh et al. 2017). This work will analyze the emission as a whole, from an active source varying its flux and morphology in tandem with the associated ARTB.

2.1. Coevolution of Source Parameters

Figure 2 presents the temporal evolution of integrated flux density and median-subtracted position angle (hereafter, position angle) of the source with its area during various phases. The data presented for the pre-flare phase is from a period devoid of strong bursts; the flare phase sample data is from a period of intense bursts; and the post-flare phase data is from a period well after the radio flux dropped. The integrated flux density, area, and position angle of the noise storm source show rapid variability with occasional strong pulses. These parameters also show periods of correlated evolution in all phases. For example, in the pre-flare phase, area and integrated flux density show an anticorrelation in the first ≈8 s. Later, they evolve correlated with a common peak around 18 s. Beyond 25 s the floor of the integrated flux density rises steadily, but the area varies around a fixed floor. Their coevolutionary trend seems erratic in this phase. A similarly erratic nature is seen in

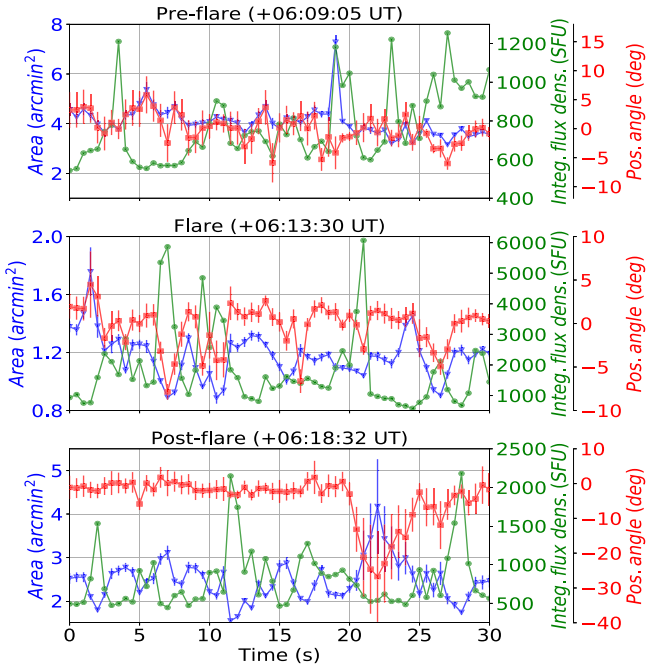

Figure 2. Coevolution of integrated flux density, area, and position angle during different phases, within a 30 s window. The plotted data come from the mid frequency of the respective bands. Start time of each set of data is given in the title.

position angle and area coevolution in the post-flare phase. When the first ≈10 s give an impression that the two parameters are correlated, their trends dissociate around 15 s and become anticorrelated beyond 20 s. However, in the flare and post-flare phases the anticorrelated evolution of area and integrated flux density is evident. Similarly, area and position angle show a correlated evolution in the pre-flare and flare phases. To get a clear picture of coevolution of these parameters in each phase, a normalized cross-correlation (NCC) analysis was carried out. Source area was chosen as the base parameter with which the others where correlated. NCC functions were evaluated for each pair of parameters, at every observation frequency, by correlating their full time profiles at 0.5 s cadence in each phase. Figure 3 shows the NCC matrices truncated at ±2 minutes. The observation frequencies with a significant amount of masked data were excluded in this analysis. The NCC functions are quite similar across the band. Hence a representative band averaged NCC (⟨NCC⟩) was computed. Assuming the coronal density model by Zucca et al. (2014), the 15 MHz (30 MHz) band corresponds to a region less than 10% (14%) of the pressure scale height of the local corona. So, the mean physical and dynamical properties are expected to be similar across this band, as seen in the NCC functions. Extending the same argument, since the central frequencies of the observation bands differ only by 30 MHz, ⟨NCC⟩ for all phases belong to the same coronal region. This work presents the discovery of correlated evolution in the three "independent" parameters that define a noise storm source.

3. Discussion

Analysis of the effects of radiowave scattering and imaging artifacts in the observed trends confirms their noise storm source origin. It also reveals that, despite the coevolution, the values of the parameters show no definitive trends among each other (see the Appendix). M19 showed that the noise storm source is part of a large loop structure and is dynamically linked to a small active region loop via a common magnetic footpoint (M19 Figure 11). The small loop underwent an ARTB during the flare phase, simultaneously enhancing the noise storm activity. The EUV analysis of the ARTB region revealed a braided structure at ≈12 Mm scale during the flare. The magnetic stresses continuously built up across the braid could have been released via enhanced particle acceleration events, causing the rise in radio flux. The radio light curve showed 30 s QPPs, which became more regular during the ARTB (Figure 1). The Alfvén speed estimate (0.4 Mm s^{-1}) from the magnetic field modeling and the QPP period provide a length scale of 12 Mm in the radio source region. This matches the braiding scale at the ARTB site. So, M19 suggested that the radio source and the ARTB region are probably driven by their common footpoint, leading to the braiding of local loop structures at similar scales. The bright type-I bursts seen in SPREDS are clumped within 30 s periods, which made the authors propose a periodic excitation of particle acceleration episodes like an avalanche within the local Alfén timescale as the braided loops relaxed their excess internal energy continuously pumped in from below. The absence of trends between any two source parameter values, support the picture of random particle acceleration episodes with differing scales as part of an avalanche. Figure 4 shows the evolution of area, integrated flux density, and position angle of the true source, averaged across the band during different phases. The data were smoothed by a 30 s running mean filter. Vertical lines are marked every 30 s. I report the discovery of 30 s QPPs in the area and position angle of the noise storm source, in tandem with its integrated flux density. This strengthens the hypothesis of a braid that relaxes at Alfvén timescales. The correlated evolution of the true source parameters and the QPPs will now be analyzed based on the above picture.

3.1. Nature of Correlated Evolution and Its Implications

From Figure 3, it is inferred that there are two dominant modes of correlated evolution in source parameters: an area–position angle correlated mode ("T" mode hereafter) and an area-integrated flux density anticorrelated mode ("S" mode hereafter). The source area is a proxy to the size of the region of instability driven by accelerated electron beams produced at particle acceleration sites, that are magnetically linked to the noise storm source region. The source position angle is a proxy to the direction or tilt of the propagating beams and the integrated flux density relates to the beam energy flux density. So, "S" mode can be envisaged as a sausage like mode where the area of the instability region and the energy flux density of the beam electrons are anticorrelated. Similarly, "T" mode is akin to a winding−unwinding mode like the illustration in Figure 4(d) where size and orientation of the electron beam varies in a correlated manner as the braid switches from a tight to loose winding configuration. Figures 4(a)–(c) shows 30 s running mean filtered trends for each parameter. Simultaneous 30 s QPPs are found in all parameters. These QPPs show correlated evolutionary trends consistant with the dominant mode in each phase. The type-I bursts that are clumped within the 30 second periods also show the same coevolutionary behavior (Figures 2 and 4). This could be because the accelerated beams causing the bursts are jointly releasing the excess energy accumulated within Alfvén (QPP) timescales in

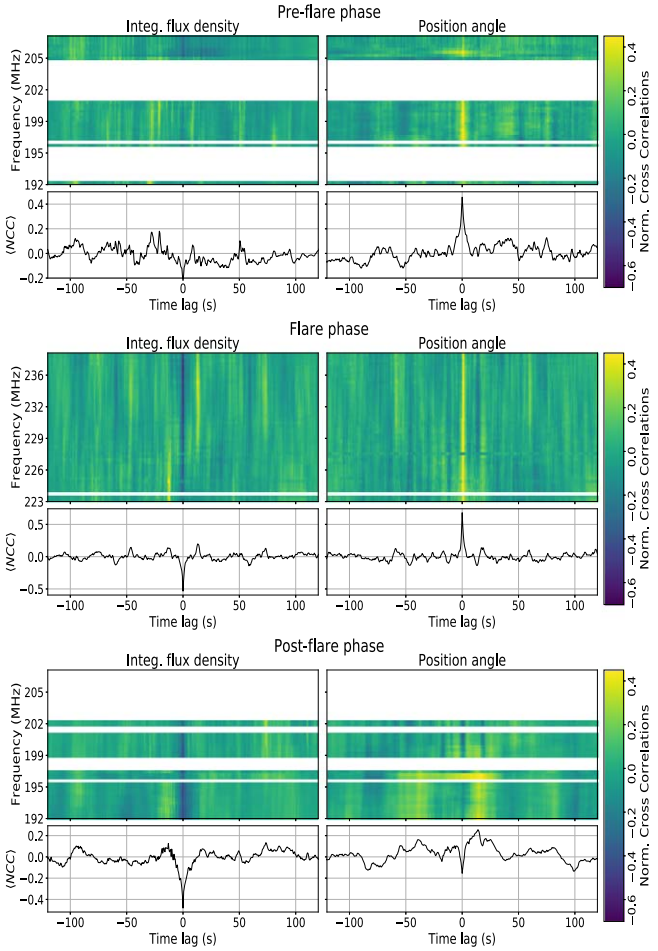

Figure 3. Matrix plots present the NCC functions for integrated flux density (left) and position angle (right) of the source with respect to its area, for every observation frequency during different phases. The masked bands had many data gaps. The line plot below each matrix plot is the band averaged NCC (⟨NCC⟩).

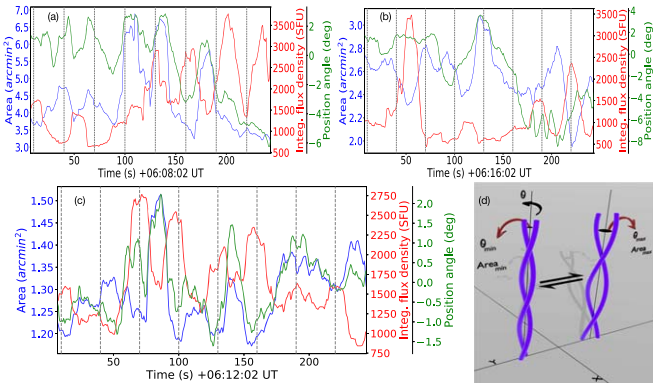

Figure 4. Panels (a)–(c): band averaged light curves of area, integrated flux density, and position angle of the true source after applying a 30 s running mean filter. Vertical lines are marked every 30 s. Panel (d): "T" mode schematic showing the correlated evolution of area and position angle (θ) as a braid wind/unwind. The subscript min/max indicates the relative parameter values.

some mode ("T" and/or "S") across the local dominant braid. The noise storm continuum could be comprised of numerous unresolved low energy bursts. "T" mode dominates in the pre-flare phase. The flare phase marks the rise of "S" mode alongside "T", which gives way for "S" in the post-flare phase. This hints at a conversion in the dominant mode via the flare. The possible physical implications will now be discussed.

3.1.1. Pre-flare Phase

The physical picture put forth by M19 suggests that the fast twisting motion in the magnetic strands driven by the footpoint motions causes the energy build up primarily in the "T" mode. Sausage like "S" mode is absent in this phase. The dominant braided structure becomes unstable at an Alfvén timescale of 30 s and releases the excess energy via an avalanche of reconnection events producing accelerated electron beams. These cause the observed bursts with the "T" mode imprinted.

3.1.2. Flare and Post-flare Phase

The "T" mode enhanced in the flare phase, possibly due to the twisting of already critically braided field structures. Simulations show that this can cause kink instabilities in the loop and the excess energy gets released as accelerated particle beams and local heating, followed by gradual internal restructuring (e.g., Gordovskyy & Browning 2012; Threlfall et al. 2018). ARTB and the X-ray flare are signs of heating. The radio flux hike could be due to increased particle acceleration events. The rise of "S" mode during flare phase is noteworthy. All these hint at a redistribution of the excess "T" mode energy to other degrees of freedom. In the post-flare phase the "T" mode gives way to "S". This mode conversion is possibly a sign of a restructuring loop.

Earlier studies on internally twisted loops targeted flares with strong hard X-ray and microwave emission, for measurements with good signal-to-noise ratios (e.g., Gordovskyy et al. 2012, 2020; Sharykin et al. 2018). Here, a new way is presented to study such loops by tracking the dominant modes of evolution in the associated bright noise storm sources, and thereby help bypass the constraint on flare energy.

4. Conclusions

The coevolution of source area, sky-orientation, and integrated flux density of a noise storm, associated with an ARTB (microflare) is presented. This work presents the discovery of simultaneous and often correlated variations in these parameters. Correlated QPPs in area, position angle, and flux density of the noise storm source are also discovered. NCC analysis between the parameters during the pre-flare, flare, and post-flare phases revealed two dominant modes of correlated evolution: area-integrated flux density anticorrelated mode, named "S" mode, like a sausage mode; area–position angle correlated mode, named "T" mode, like a winding-unwinding mode. A conversion in the dominant mode from "T" to "S" is discovered, mediated by the flare. This can be a signature of the release of excess magnetic stress energy built up in "T" mode in the local coronal loops, during the flare. Eventually, the "T" mode energy density is redistributed to "S" mode and particle energy. Such mode evolution patterns in associated noise storm sources can be used as diagnostics to study the evolution of flaring loops, regardless of flare energy.

This scientific work makes use of the Murchison Radio-astronomy Observatory (MRO), operated by the Commonwealth Scientific and Industrial Research Organisation (CSIRO). We acknowledge the Wajarri Yamatji people as the traditional owners of the Observatory site. Support for the

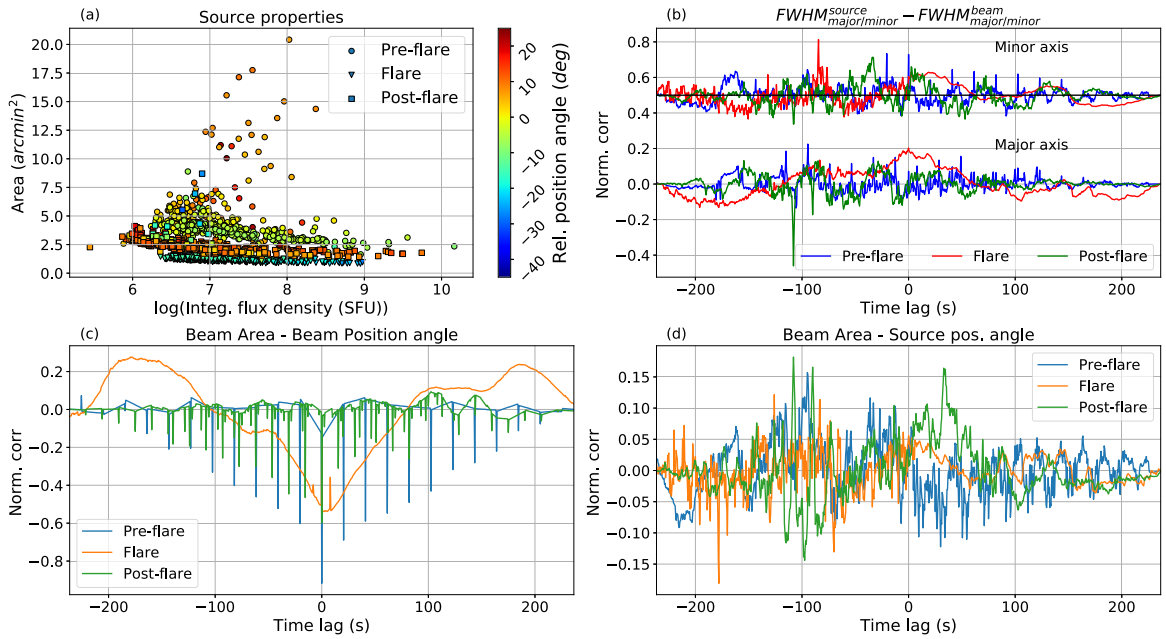

Figure 5. Panel (a): area vs. integrated flux density of the true source. The position angle of the true source relative to the beam is color coded. Panel (b): NCC function for the true source and the beam minor axes widths (Above) and major axes widths (Below). NCC values for minor axes are shifted by 0.5 for visual clarity. Panels (c)–(d): NCC functions for the area and position angle of the beam (c), and for the beam area and the true source position angle (d).

operation of the MWA is provided by the Australian Government's National Collaborative Research Infrastructure Strategy (NCRIS), under a contract to Curtin University administered by Astronomy Australia Limited. We acknowledge the Pawsey Supercomputing Centre, which is supported by the Western Australian and Australian Governments. This work is supported by the Research Council of Norway through its Centres of Excellence scheme, project Number 262622 ("Rosseland Centre for Solar Physics"). A.M. acknowledges support from the EMISSA project funded by the Research Council of Norway (project number 286853). A.M. acknowledges Olga Mohan for the graphical support. A.M. acknowledges Prof. Divya Oberoi, Surajit Mondal, and the anonymous referee for useful discussions. This research made use of NASA's Astrophysics Data System (ADS).

Facilities: MWA, SDO(AIA), RHESSI and GOES.

Software: Numpy (Harris et al. 2020), Astropy (Astropy Collaboration et al. 2013), Matplotlib (Hunter 2007), CASA (McMullin et al. 2007), Sunpy (Community et al. 2015).

Appendix
Analysis of the Effects of Scattering and Imaging Artifacts

The effect of radiowave scattering and the possible imaging artifacts in the observed parameter evolution will be discussed here. Scattering changes the absolute source size, as a convolution by a Gaussian scatter function, the width of which depends on the mean statistical properties of the ambient plasma (Arzner & Magun 1999; Kontar et al. 2017; Mohan et al. 2019b). The noise storm source region is located at around $1.14\,R_\odot$ when the ARTB source was at $\approx 1.02\,R_\odot$ (see Figure 11 in M19). Though magnetically connected, the regions are spatially so far apart for the ARTB to have varied the ambient density fluctuation index ($\delta N/N$) at the noise storm region, sufficient enough to cause the observed large fractional changes in its area by about a few to $\approx$100% within spans of a few seconds (Figure 2). Hence, the role of scattering in the observed source variability can be discarded. The noise storm sources are well described by a single 2D Gaussian morphology. The low errors in the derived quantities, shown in Figure 2, testify this. The errors in position angle appear large, as the plotted data are median subtracted. However, in reality there could be multiple sources that are unresolved by MWA and(or) are smeared by scattering. But this study focuses on the overall effective size and shape of the radio source, which is well captured by the Gaussian fitting procedure.

Though MWA is a dense compact array with 8128 baselines within the 100–3000 m range (Tingay et al. 2013), since the true source sizes are smaller than the beam extent, any possible systematic effects due to beam structure variations or angular resolution should be studied. Imaging at every time and frequency bin is an independent process with a unique beam shape. Still, the true source parameter trends look similar across frequency for the entire observation period. This increases the odds of them being intrinsic. Figure 5(a) shows various analysis done for the mid-band data during various observation phases. The choice of mid-band is arbitrary and it is expected that the imaging artifacts, if any, due to the issue of source size should be of the same statistical nature at all frequencies. This is because the source sizes and imaging procedure are similar across the band. Color coded are the true source position angle at each instant after subtracting the corresponding beam position angle. There is no significant trend among parameters, especially in the mid ranges of their values, which are unaffected by any bias due to low event counts. If some systematic effects had seeped into the true source structure due to its relatively small size, the true source dimensions derived would have systematically mimicked the beam with relative position angle tending to zero toward small area values. Figure 5(b) shows the NCC for the FWHM of minor axes of the beam and the true source in the top. NCC values are hiked by 0.5 for representative purposes and the black horizontal line at 0.5 marks the true NCC = 0 line. Similar analysis for major axes is shown below. There is no correlation between the

angular scales of the true source and the beam even in the flare phase, when source sizes were relatively smaller. Figure 5(c) shows the NCC for the area and position angle of the beam. There is no sign of correlation during any observation phase, unlike the true source data. On the contrary, it shows spikes in pre-flare and post-flare phases and an anticorrelation prominent in flare phase. These spikes resulted since the imaging pipeline performed fresh calibration runs on the data every $\approx$20 s leading to different antenna flagging schemes, which affected the beam structure. The solution from each calibration run was applied to make images in the intermediate time steps. In the flare phase, since the source is very bright, high dynamic range images could be obtained with just a few rounds of self-calibration after applying calibration solutions from the initial time slice. Figure 5(d) shows the NCC between beam area and true source position angle, which shows no sign of correlated evolution in any phase, unlike the NCC of the true source data. These results increase the confidence in the observed true source area—position angle trends and assure that they are not beam-driven.

ORCID iDs

Atul Mohan https://orcid.org/0000-0002-1571-7931

References

Arzner, K., & Magun, A. 1999, A&A, 351, 1165
Astropy Collaboration, Robitaille, T. P., Tollerud, E. J., et al. 2013, A&A, 558, A33
Community, T. S., Mumford, S. J., Christe, S., et al. 2015, CS&D, 8, 014009
Elgarøy, E. Ø. 1977, Solar Noise Storms (Oxford: Pergamon Press)
Ellingson, S. W., Taylor, G. B., Craig, J., et al. 2013, ITAP, 61, 2540
Elgaroy, O., & Ugland, O. 1970, A&A, 5, 372
Fyfe, L. E., Howson, T. A., & De Moortel, I. 2020, A&A, 643, A86
Ginzburg, V. L., & Zhelezniakov, V. V. 1958, SvA, 2, 653
Gordovskyy, M., & Browning, P. K. 2012, SoPh, 277, 299
Gordovskyy, M., Browning, P. K., Inoue, S., et al. 2020, ApJ, 902, 147
Gordovskyy, M., Browning, P. K., Kontar, E. P., & Bian, N. H. 2012, SoPh, 284, 489
Guedel, M., & Benz, A. O. 1990, A&A, 231, 202
Harris, C. R., Millman, K. J., van der Walt, S. J., et al. 2020, Natur, 585, 357
Hunter, J. D. 2007, CSE, 9, 90
Iwai, K., Misawa, H., Tsuchiya, F., et al. 2012, in ASP Conf. Ser. 454, Hinode-3: The 3rd Hinode Science Meeting, ed. T. Sekii, T. Watanabe, & T. Sakurai (San Francisco, CA: ASP), 249
Iwai, K., Miyoshi, Y., Masuda, S., et al. 2011, ApJ, 744, 167
Iwai, K., Miyoshi, Y., Masuda, S., et al. 2014, ApJ, 789, 4
James, T., & Subramanian, P. 2018, MNRAS, 479, 1603
Kassim, N., White, S., Rodriquez, P., et al. 2010, in Proc. Advanced Maui Optical and Space Surveillance Technologies Conf., ed. S. Ryan (Maui, HI: The Maui Economic Development Board), E59
Kathiravan, C., Ramesh, R., & Nataraj, H. S. 2007, ApJL, 656, L37
Kontar, E. P., Yu, S., Kuznetsov, A. A., et al. 2017, NatCo, 8, 1515
Le Squeren, A. M. 1964, in AAS-NASA Symp.,The Physics of Solar Flares, ed. W. N. Hess (Washington, DC: NASA, Science and Technical Information Division), 199
Li, C. Y., Chen, Y., Wang, B., et al. 2017, SoPh, 292, 82
McMullin, J. P., Waters, B., Schiebel, D., Young, W., & Golap, K. 2007, in ASP Conf. Ser. 376, Astronomical Data Analysis Software and Systems XVI, ed. R. A. Shaw, F. Hill, & D. J. Bell (San Francisco, CA: ASP), 127
Melrose, D. B., & Sy, W. N. 1972, AuJPh, 25, 387
Mercier, C., & Trottet, G. 1997, ApJL, 474, L65
Mohan, A., McCauley, P. I., Oberoi, D., & Mastrano, A. 2019a, ApJ, 883, 45
Mohan, A., Mondal, S., Oberoi, D., & Lonsdale, C. J. 2019b, ApJ, 875, 98
Mohan, A., & Oberoi, D. 2017, SoPh, 292, 168
Mondal, S., Mohan, A., Oberoi, D., et al. 2019, ApJ, 875, 97
Sharykin, I. N., Kuznetsov, A. A., & Myshyakov, I. I. 2018, SoPh, 293, 34
Shimizu, T., Tsuneta, S., Acton, L. W., Lemen, J. R., & Uchida, Y. 1992, PASJ, 44, L147
Smith, E. V. P., & McIntosh, P. S. 1962, JGR, 67, 1013
Sundaram, G. A. S., & Subramanian, K. R. 2005, MNRAS, 359, 580
Suresh, A., Sharma, R., Oberoi, D., et al. 2017, ApJ, 843, 19
Threlfall, J., Hood, A. W., & Browning, P. K. 2018, A&A, 611, A40
Tingay, S. J., Goeke, R., Bowman, J. D., et al. 2013, PASA, 30, e007
van Haarlem, M. P., Wise, M. W., Gunst, A. W., et al. 2013, A&A, 556, A2
Wild, J. P. 1957, in IAU Symp. 4, Radio Astronomy, ed. H. C. van de Hulst (Cambridge: Cambridge Univ. Press), 321
Zucca, P., Carley, E. P., Bloomfield, D. S., & Gallagher, P. T. 2014, A&A, 564, A47